



# Suppression of nano-hydride growth on Nb(100) due to nitrogen doping

Cite as: J. Chem. Phys. 152, 214703 (2020); <https://doi.org/10.1063/5.0007042>

Submitted: 08 March 2020 . Accepted: 03 May 2020 . Published Online: 01 June 2020

R. Darren Veit, Rachael G. Farber , Nathan S. Sitaraman, Tomas A. Arias, and S. J. Sibener 



View Online



Export Citation



CrossMark

Lock-in Amplifiers  
up to 600 MHz



# Suppression of nano-hydride growth on Nb(100) due to nitrogen doping

Cite as: J. Chem. Phys. 152, 214703 (2020); doi: 10.1063/5.0007042

Submitted: 8 March 2020 • Accepted: 3 May 2020 •

Published Online: 1 June 2020



View Online



Export Citation



CrossMark

R. Darren Veit,<sup>1</sup> Rachael G. Farber,<sup>1</sup>  Nathan S. Sitaraman,<sup>2</sup> Tomas A. Arias,<sup>2</sup> and S. J. Sibener<sup>1,a)</sup> 

## AFFILIATIONS

<sup>1</sup>The James Franck Institute and Department of Chemistry, The University of Chicago, 929 E. 57th Street, Chicago, Illinois 60637, USA

<sup>2</sup>Department of Physics, Cornell University, 109 Clark Hall, Ithaca, New York 14853, USA

<sup>a)</sup>Author to whom correspondence should be addressed: [s-sibener@uchicago.edu](mailto:s-sibener@uchicago.edu)

## ABSTRACT

Niobium superconducting radio frequency (SRF) cavities enable the operation of modern superconducting accelerator facilities. These cavities do not approach the theoretical performance limits of Nb due to the deleterious effects of surface defects and chemical inhomogeneities such as Nb hydrides. Nitrogen doping is known to consistently increase the cavity performance and inhibit Nb hydride growth, but a comprehensive understanding of Nb hydride growth and suppression is not yet realized. Scanning tunneling microscopy (STM), scanning tunneling spectroscopy (STS), and density functional theory (DFT) calculations presented herein elucidate the real-time, nanoscale structural and electronic evolution of undoped, hydrogen doped, and hydrogen and nitrogen doped Nb(100) due to the growth and suppression of Nb nano-hydrides. DFT calculations in agreement with the experimental data found unique near-surface phases stabilized upon dopant incorporation. The experimental STM and STS results and DFT calculations reported herein provide the first *in situ* and real-time nanoscale visualization and characterization of the effects of nitrogen doping on Nb hydride suppression and growth. Such information allows for further optimization of nitrogen doping procedures and advances in the performance of SRF materials for next-generation SRF-based accelerators and free electron lasers.

Published under license by AIP Publishing. <https://doi.org/10.1063/5.0007042>

## I. INTRODUCTION

Particle accelerators are widely used in fundamental research as well as industrial and medical applications. Superconducting radio frequency (SRF) cavities are the key enabling technology to modern superconducting accelerators; advances in SRF technology are necessary to achieve more powerful and efficient accelerators.<sup>1,2</sup> The current standard material for SRF cavities is Nb [critical temperature ( $T_c$ ) of 9.25 K]<sup>2–4</sup> due to its ultra-low surface resistance ( $R_s$ ) and high quality factor ( $Q$ ) at operating temperatures of  $\sim 2$  K.<sup>1</sup> The structural and chemical composition of the Nb SRF cavity surface is crucial; the electromagnetic field penetrates  $\sim 100$  nm due to the skin effect, where the current density is largest in the near-surface of superconducting materials under operating conditions. Consequently, previous work has investigated the relationship between surface morphology,<sup>3,5–7</sup> defects,<sup>8–12</sup> contaminant incorporation,<sup>8–10,13</sup> and processing procedures<sup>3,11</sup> on the superconducting properties of Nb SRF cavities.

A significant source of SRF cavity performance loss is due to Nb hydrides.<sup>14–17</sup> Nb readily absorbs hydrogen when the bulk oxide ( $\text{Nb}_2\text{O}_5$ ) is removed from the surface.<sup>14,16</sup> During fabrication, the cavity is polished via buffered chemical polishing (BCP), electropolishing (EP), or centrifugal barrel polishing (CBP), removing the  $\text{Nb}_2\text{O}_5$  layer, resulting in significant hydrogen absorption.<sup>18</sup> At 300 K, the absorbed hydrogen occupies interstitial sites throughout the cavity.<sup>15</sup> Upon cooling, the hydrogen precipitates as micrometer-scale Nb hydrides on the cavity surface with nucleation and growth temperatures between  $\sim 70$  K and 170 K.<sup>14,16</sup> Nb hydrides are non-superconducting at  $T > 1.3$  K<sup>15</sup> and result in a significant decrease in  $Q$  due to local surface heating; this phenomenon has been dubbed the “hydrogen  $Q$  disease.”<sup>19–21</sup> While degassing cavities under ultra-high vacuum conditions at 1100 K effectively degasses most of the incorporated hydrogen and mitigates the hydrogen  $Q$  disease, residual hydrogen precipitates out as nano-hydride species.<sup>14–17</sup>

In an effort to mitigate the effects of deleterious hydrogen species, the beneficial effect of intentionally incorporated impurities,

such as nitrogen, oxygen, and carbon, on  $R_S$  and  $Q$  has been previously studied.<sup>6,7,22–28</sup> Nitrogen doping (N-doping) has emerged as a promising method to limit hydride precipitation, reliably increasing  $Q$  and reversing the  $Q$  field dependence in the medium field regime.<sup>8,10,29–34</sup> This is achieved due to the attenuation of the electron mean free path upon the incorporation of nitrogen within the depth of the RF penetration layer.<sup>1,35–37</sup> While the mechanisms linking a shortened electron mean free path to decreased surface resistance are not yet realized, there is evidence that a shorter electron mean free path beneficially impacts the surface resistance of SRF materials, leading to improved SRF cavity performance.<sup>35</sup> In addition to the attenuated electron mean free path, first-principles calculations suggest that nitrogen interstitials increase the barrier to hydrogen diffusion, effectively trapping hydrogen in the bulk and preventing Nb hydride precipitation more effectively than interstitial, or dissolved, oxygen in the near-surface.<sup>29,30,33,38</sup> Carbon, while less studied than previously mentioned interstitial impurities, has been shown to have unique behavior in Nb interstitial sites.<sup>39–41</sup> While hydrogen is shown to aggregate at defects in Nb SRF cavities, bonding with Nb in an extended Nb–H network, carbon interstitials preferentially form C–C dimers around Nb defects. In this way, carbon does not form an extended Nb–C phase, but rather forms C–C dimers in Nb lattice vacancies.<sup>39</sup> While C–H bonds are not favored, there is evidence that a carbon atmosphere forms at defect sites, potentially interfering with the ability for hydrogen to diffuse to such defect sites and propagate the growth of Nb hydrides.

In addition to the evolving understanding of interstitial species influence on the performance of Nb SRF cavities, there has been a progression in N-doping procedures. The N-doping procedure for Nb SRF cavities developed by Grassellino *et al.*<sup>8</sup> relies on holding a 1.3 GHz TESLA shaped fine-grain Nb SRF cavity at  $\sim 1273.5$  K with  $\sim 20$  mTorr  $N_2$ . This higher temperature doping procedure, significant in the initial identification of nitrogen as a beneficial interstitial species, has allowed for the further development of N-doping techniques such as the “low temperature nitrogen infusion” preparation method identified by Grassellino *et al.*<sup>32</sup> This preparation method exposes Nb SRF cavities to  $\sim 25$  mTorr  $N_2$  for 2 min at 393.5 K–473.5 K. The implementation of the low temperature nitrogen infusion method has resulted in Nb SRF cavities with higher  $Q$  and lower  $R_S$  when compared to higher temperature N-doping methods.

Despite the work done to identify the effects of dopants on Nb SRF cavities,<sup>24,25,42,43</sup> little is understood regarding the incipient, nano-scale growth and suppression behavior of Nb hydrides. In this work, we have used single-crystal Nb(100) to investigate the initial, nano-scale structural evolution of Nb(100) as a function of Nb nano-hydride precipitation and growth. Time-lapse low-temperature scanning tunneling microscopy (LT-STM) imaging of hydrogen doped Nb(100) demonstrated real-time structural evolution with nano-scale spatial resolution, and scanning tunneling spectroscopy (STS) determined the unique electronic characteristics of Nb nano-hydride surface phases; these results are supported by density functional theory (DFT) surface density of states (SDOS) calculations. We then demonstrated the successful suppression of Nb nano-hydrides, following nitrogen and hydrogen co-doping in Nb(100) via LT-STM. STS confirmed the presence of unique surface electronic characteristics with both nitrogen and

hydrogen in the near surface of Nb(100) as supported by DFT SDOS calculations. These results provide the first structural and electronic evolution of Nb(100) as a function of initial nano-hydride growth and suppression.

## II. EXPERIMENTAL

Experiments were performed on a Nb(100) single crystal (Surface Preparation Laboratory) in a UHV system equipped with a scanning tunneling microscopy chamber (UHV VT-STM, RHK Technology) and preparation chamber, as previously described.<sup>44</sup> The crystal was cleaned via repeated cycles of  $Ar^+$  ion sputtering and annealing at a sample temperature ( $T_{\text{sample}}$ ) of 2100 K, measured using an infrared pyrometer (Mikron Infrared, MG-140). Surface cleanliness was confirmed with Auger electron spectroscopy (AES), x-ray photoelectron spectroscopy (XPS), and STM analysis.

Hydrogen and nitrogen exposures, and temperature programmed desorption (TPD) measurements, were carried out in the preparation chamber. Following the formation of the pristine ( $3 \times 1$ )-O surface,<sup>44–46</sup> hydrogen doped (H-doped) samples were prepared by holding the crystal at  $T_{\text{sample}} = 800$  K and backfilling the preparation chamber to  $5.5 \times 10^{-5}$  Torr  $H_2$  for 20 min. Hydrogen uptake was quantified with TPD measurements, and there was no evidence of background gas accumulation or surface degradation during prolonged STM experiments, as confirmed by TPD. To produce the nitrogen and hydrogen doped (co-doped) surface, the ( $3 \times 1$ )-O sample was held at  $T_{\text{sample}} = 1100$  K, the temperature at which actual Nb SRF cavities are held during N-doping.<sup>8</sup> The preparation chamber was backfilled to 20 mTorr  $N_2$  for 10 min.  $T_{\text{sample}}$  was then reduced to 800 K, and the preparation chamber was backfilled to  $1.0 \times 10^{-4}$  Torr  $H_2$  for 20 min. Co-doped TPDs taken prior to the STM experiments were identical to those taken after prolonged STM experiments.

STM and scanning tunneling spectroscopy (STS) data were collected using LT-STM cooled with a continuous flow liquid helium cryostat to maintain an STM stage temperature ( $T_{\text{STM}}$ ) of 100 K. STM and STS measurement reproducibility was confirmed by analyzing multiple undoped, H-doped, and co-doped samples in a randomized order. In addition to repeated trials of identical sample preparation methods, each sample was analyzed via STM and STS at multiple locations across the face of the Nb(100) sample. As such, the STM and STS data reported herein are representative of the surface structures and  $dI/dV$  data collected during this study. The structural evolution and  $dI/dV$  spectra were consistent for each respective sample preparation, regardless of the STM tip used for measurement.

In summary, sample preparation for the undoped, H-doped, and co-doped samples discussed herein is as follows:

1. Undoped Nb(100): Repeated sputtering and annealing cycles, as reported in previous work,<sup>44</sup> to form the pristine ( $3 \times 1$ )-O surface, as confirmed by AES and STM analysis.
2. H-doped Nb(100): The pristine ( $3 \times 1$ )-O surface was held at  $T_{\text{sample}} = 800$  K and exposed to  $5.5 \times 10^{-5}$  Torr  $H_2$  for 20 min.
3. Co-doped Nb(100): The pristine ( $3 \times 1$ )-O surface was held at  $T_{\text{sample}} = 1100$  K and exposed to 20 mTorr  $N_2$  for 10 min.  $T_{\text{sample}}$  was then reduced to 800 K and exposed to  $1.0 \times 10^{-4}$  Torr  $H_2$  for 20 min.

For all Nb hydride growth experiments, the undoped, H-doped, and co-doped Nb(100) samples were analyzed via STM and STS at  $T_{\text{STM}} = 100$  K for  $\sim 72$  h to capture the Nb hydride-induced surface and STS evolution.

First principles electronic structure calculations within density functional theory (DFT) were used to calculate STS fingerprints for candidate surface structures.<sup>47</sup> A standard symmetric surface-slab periodic supercell representation, consisting of 7–9 layers of Nb atoms capped with  $(3 \times 1)$ -O surface oxide (Fig. 1) with varying amounts of additional interstitial oxygen, nitrogen, and hydrogen atoms, was used. For comparison with the experimentally determined surface density of states (SDOS), as inferred through the standard  $(dI/dV)/(I/V)$  scheme,<sup>48</sup> we computed the local electronic density of states integrated to a depth of 1.5 Å below the uppermost atom with a Wannier functional based technique, described below. The appropriate slab thickness was determined by converging our calculated SDOS with respect to the thickness.

In order to capture the long-range strain effect arising from the 10% lattice mismatch between Nb and NbO, the lattice vectors of the native  $(3 \times 1)$ -O surface oxide were taken to be 9.86 Å and 3.09 Å, where 3.09 Å is chosen to fall between the calculated NbO lattice constant of 2.99 Å and the calculated Nb lattice constant of 3.29 Å, in best agreement with experimental evidence.<sup>45,46</sup> For the undoped  $(3 \times 1)$ -O surface, structures with 5–9 oxygen atoms per  $(3 \times 1)$  cell were considered. For the H-doped and N-doped surfaces, we considered hydride and nitride phases beneath the oxide, as well as several possible configurations of interstitial hydrogen and nitrogen, and substitutional nitrogen.

To determine the local DOS, we employ a Wannier function based-method.<sup>49</sup> The electronic structure for a given surface structure was first transformed into a maximally localized Wannier function basis, which was then used to calculate eigenvalues weighted based on the overlaps of Wannier functions with the surface region of interest. These were smoothed with an energy width of 0.1 eV to account for the broadening of the electronic states, an estimate based on the known mean free path of about 5 nm and Fermi velocity of  $\sim 6 \times 10^5$  m/s in impurity-rich niobium.<sup>35,50</sup> The DOS was produced by summing the resulting broadened energy levels within binned energy ranges.

Finally, the *ab initio* electronic structure was calculated using the Perdew–Burke–Ernzerhof (PBE) version of the

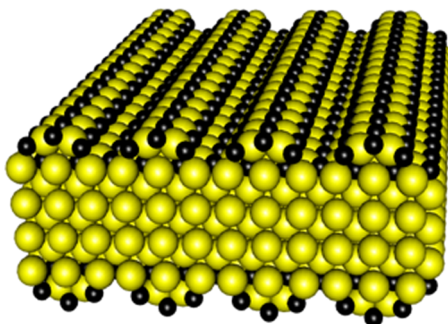


**FIG. 1.** Nb(100)  $(3 \times 1)$ -O slab used for density functional theory utilizing a standard symmetric surface-slab periodic supercell with 7–9 layers of Nb atoms capped with NbO.

generalized-gradient approximation (GGA) to DFT.<sup>51</sup> Calculations were performed in a plane-wave basis with ultrasoft pseudopotentials,<sup>52</sup> an energy cutoff of 12 hartree. Most calculations were performed on the  $(3 \times 1)$  unit cell with a  $4 \times 12$  k-point mesh, while calculations involving hydrides were performed on a  $(6 \times 2)$  unit cell with a  $2 \times 6$  k-point mesh. A vacuum spacing of at least 7 Å was used for all calculations. An effective electron temperature of 5 millihartree was used in order to achieve good convergence of quantities of interest with a modest k-point mesh; this results in no visible change in the computed density of states compared to calculations using Marzari's cold smearing technique.<sup>53</sup> For all calculations, ionic positions were converged to an energy tolerance of  $5 \times 10^{-7}$  hartree per Nb atom, and the electronic structure was converged to an energy tolerance of  $5 \times 10^{-10}$  hartree per Nb atom.

### III. RESULTS AND DISCUSSION

Using both experimental and theoretical techniques, we show that H-doped Nb(100) undergoes extensive structural evolution on the nanoscale due to Nb nano-hydride formation. Sequentially taken LT-STM data provide real-time, nanoscale information regarding the hydride-induced surface evolution, and a corresponding shift in surface electronic characteristics is observed via STS. Co-doped Nb(100) analyzed via LT-STM and STS shows unique surface electronic characteristics as a result of incorporated nitrogen. Experimental STS data for all samples are supported with DFT calculations for the SDOS and provide insight into the hydride and nitride phases that contribute to the observed structural and electronic evolution.

### IV. HYDROGEN AND NITROGEN INCORPORATION

It is known that the bulk pentoxide, Nb<sub>2</sub>O<sub>5</sub>, is ever-present under ambient conditions, and removal of Nb<sub>2</sub>O<sub>5</sub> requires annealing under UHV conditions.<sup>46,54–57</sup> Annealing below  $\sim 1900$  K results in oxygen dissolution, resulting in formation of NbO<sub>2</sub> and NbO.<sup>6,58,59</sup> It is only upon annealing above  $\sim 1900$  K that oxygen desorbs from Nb as NbO and NbO<sub>2</sub> species and complete oxygen removal can only be achieved by annealing Nb under UHV conditions above 2500 K.<sup>5,6,58,60,61</sup> As such, Nb(100) is terminated by a  $(3 \times 1)$ -O NbO surface oxide<sup>44–46</sup> and is a benchmark for surface structure evolution in this work. Prior to H-doping, TPD analysis confirms that the undoped Nb(100) crystal shows no appreciable hydrogen or nitrogen desorption from 800 K–1300 K and 1000 K–2000 K, where hydrogen and nitrogen, respectively, desorb if present in the Nb bulk, as shown in Figs. 2(a) and 2(b). Following H-doping at  $T_{\text{sample}} = 800$  K and exposure to  $5.5 \times 10^{-5}$  Torr H<sub>2</sub> for 20 min, a sizable hydrogen desorption feature can be seen in the TPD in Fig. 2(c). The second temperature ramp from 1000 K–2000 K shows no appreciable nitrogen desorption, as shown in Fig. 2(d). Co-doped samples are prepared following the nitrogen incorporation procedure developed by Fermilab<sup>8</sup> with Nb(100) exposed to  $2 \times 10^{-2}$  Torr nitrogen at  $T_{\text{sample}} = 1100$  K for 10 min. TPD shows a modest nitrogen desorption feature during the 1000 K–2000 K temperature ramp, as shown in Fig. 2(f), and is consistent with the bulk desorption temperature of nitrogen from Nb of 1900 K.<sup>7</sup> Following N-doping, H-doping is accomplished with a slightly higher H<sub>2</sub> exposure partial

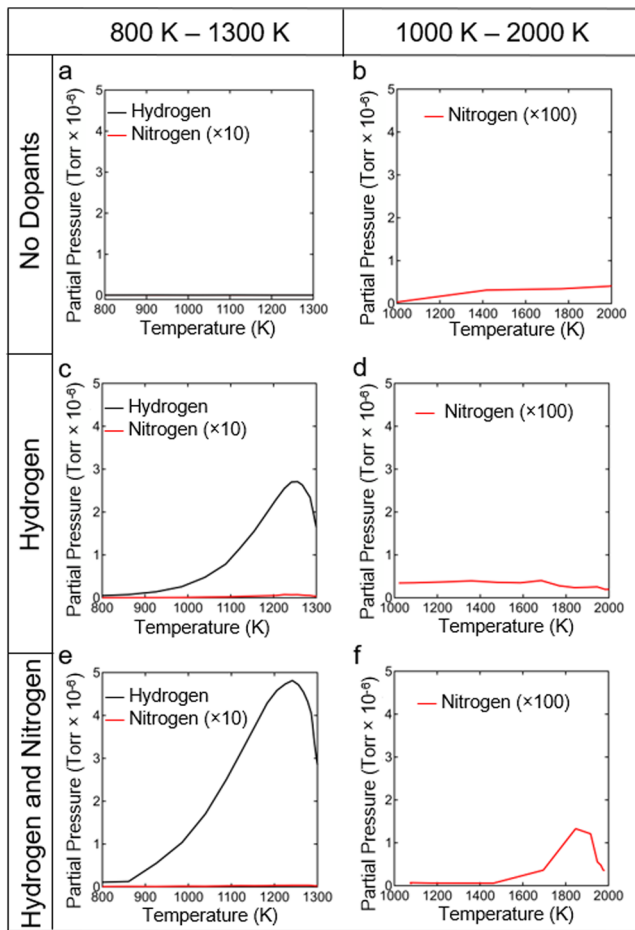


**FIG. 2.** TPD spectra of Nb(100) ( $3 \times 1$ )-O: [(a) and (b)] undoped, [(c) and (d)] H-doped, [(e) and (f)] co-doped. TPDs from 800 K–1300 K monitored hydrogen desorption and 1000 K–2000 K monitored nitrogen desorption. (a) TPD from 800 K–1300 K for the undoped sample showing no hydrogen or nitrogen uptake. (b) TPD from 1000 K–2000 K for the undoped sample showing no hydrogen or nitrogen uptake. (c) TPD from 800 K–1300 K for the H-doped sample shows a broad, intense hydrogen desorption feature. (d) TPD from 1000 K–2000 K shows no evidence of nitrogen uptake. (e) TPD from 800 K–1300 K for the co-doped sample. The hydrogen desorption feature is comparable in intensity to the H-doped sample. (f) TPD from 1000 K–2000 K for the co-doped sample shows a modest nitrogen desorption feature.

pressure of  $1.0 \times 10^{-4}$  Torr at  $T_{\text{sample}} = 800$  K for 20 min. The slightly higher  $\text{H}_2$  exposure is necessary for equivalent amounts of hydrogen per doping procedure as nitrogen appears to inhibit some hydrogen incorporation. Following co-doping, a similar hydrogen [Fig. 2(e)] and nitrogen desorption feature [Fig. 2(f)] is obtained from H-doped and N-doped samples, respectively. It is interesting to note that there is significantly less nitrogen incorporated than hydrogen. This is in agreement with recent secondary ion mass spectrometry (SIMS) results that show a very small concentration of nitrogen in the first few nanometers of the Nb cavity coupons.<sup>62</sup>

Figures 3(a)–3(c) contain STM images of the undoped, H-doped, and co-doped ( $3 \times 1$ )-O Nb(100) surface taken at room

temperature. Figure 3(a) shows pristine undoped ( $3 \times 1$ )-O ladder structures. Following hydrogen incorporation, there is no evidence of perturbation to the ( $3 \times 1$ )-O ladder structures [Fig. 3(b)]. STM images of the co-doped surface, however, as shown in Fig. 3(c), show perturbation to the native ( $3 \times 1$ )-O surface with dark defects in the ladder structure. This may be due to substitution of oxygen with nitrogen in the second layer of the NbO surface oxide, as preliminary calculations by the Arias group suggest.

## V. INITIAL ANALYSIS OF DOPED Nb(100) AT 100 K

In order to obtain structural and electronic information regarding the initial, nanoscale growth and suppression mechanisms of Nb hydrides with and without nitrogen incorporation, sequentially obtained LT-STM data were used to observe real-time structural evolution. For all LT-STM and STS analysis,  $T_{\text{STM}} = 100$  K; this  $T_{\text{STM}}$  is within the nucleation and growth range of Nb hydrides.<sup>13,15</sup>

STM measurements taken within hours of reaching equilibrium at  $T_{\text{STM}} = 100$  K for undoped [Fig. 4(a)], H-doped [Fig. 4(b)], and co-doped [Fig. 4(c)] Nb(100) show no surface evolution compared to respective room temperature data [Figs. 3(a)–3(c)]. Additionally, the STS data for each sample preparation within several hours of equilibration at  $T_{\text{STM}} = 100$  K show no deviation from the undoped Nb(100) ( $3 \times 1$ )-O surface STS [Fig. 4(d)]. The absence of structural evolution, coupled with a consistent surface DOS across all sample preparations, suggests that no Nb hydride growth has begun within several hours at  $T_{\text{STM}} = 100$  K.

Significant work has been done to elucidate the relationship between structural defects and the formation of Nb hydride species.<sup>14,16,63,64</sup> Micrometer-scale Nb hydride growth on the surface of polycrystalline Nb SRF cavity coupons occurs over the course of hours between  $\sim 100$  K–170 K.<sup>16</sup> Such a rapid growth can be attributed to the presence of crystalline defects such as Nb vacancies, dislocations, and high ( $>15^\circ$ ) and low ( $<1^\circ$ – $5^\circ$ ) angle grain boundaries (LAGBs). The work from Sung *et al.*<sup>64</sup> investigated the impact of LAGBs in Nb single crystals with a 5% tensile strain meant to mimic the processing utilized to form Nb SRF cavities. Interestingly, LAGBs within single crystal Nb serve as an effective hydride segregation site. While Sung *et al.*<sup>64</sup> reported the formation of micrometer-scale hydride growth within a Nb single crystal, the induced tensile strain introduces a number of structural defects that are not inherent to the Nb(100) crystal used in this study. As such, the unstrained Nb(100) crystal utilized herein offers significantly fewer defect sites, such as dislocations and LAGBs, to promote Nb hydride nucleation, resulting in appreciably slower nucleation and growth rates of Nb hydrides reported in this work.

## VI. ANALYSIS OF DOPED Nb(100) AT 100 K; PROLONGED COOLING

To accommodate the longer timescales for Nb hydride nucleation and growth on Nb(100), sequential LT-STM images of H-doped and co-doped Nb(100) were taken in the same location for  $\sim 72$  h. Following 24 h at  $T_{\text{STM}} = 100$  K, an area of the H-doped surface with distinct facets was selected for time-lapse imaging. In this context, a facet is defined as a point at which the surface slope changes abruptly and intersects a terrace with a significantly different slope, as shown in the inset in Fig. 5(a). The facets serve

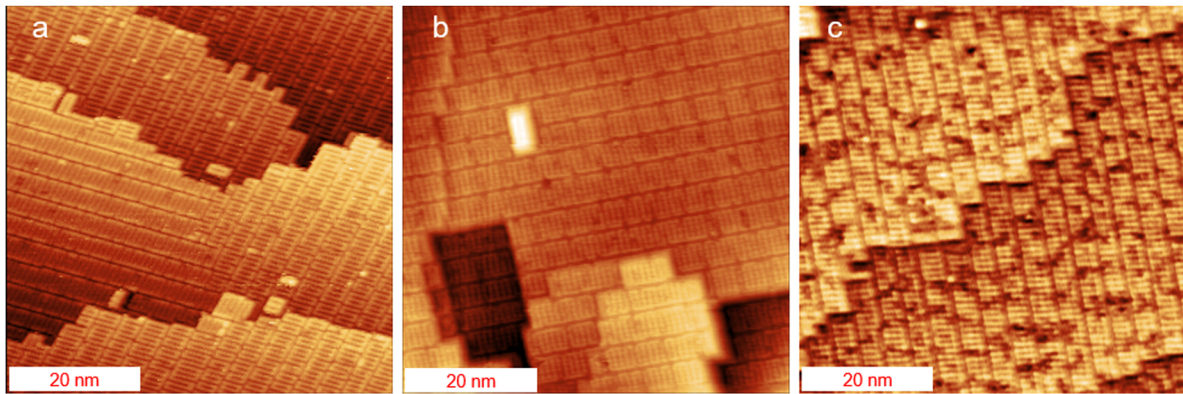


**FIG. 3.** Room temperature STM images of Nb(100)  $(3 \times 1)$ -O: (a) undoped, (b) H-doped, and (c) co-doped. Co-doping shows noticeable perturbation of the  $(3 \times 1)$ -O ladder structure. Imaging conditions: (a) 0.72 V, 99 pA; (b) 181 mV, 178 pA; and (c) -406 mV, 179 pA.

as a static positional reference point during prolonged sequential LT-STM analysis to ensure that the observed surface evolution is not a result of imaging artifacts. It is important to note that the faceted regions appeared on the Nb(100) surface as a result of surface reconstruction due to Nb nano-hydride growth. In order

to reestablish atomically flat Nb(100), prolonged sputtering and annealing cycles at  $\sim 1900$  K were needed. Such crystal treatment is in agreement with evidence of hydride-induced surface scarring that may require prolonged high temperature thermal treatments to eliminate.<sup>64</sup>

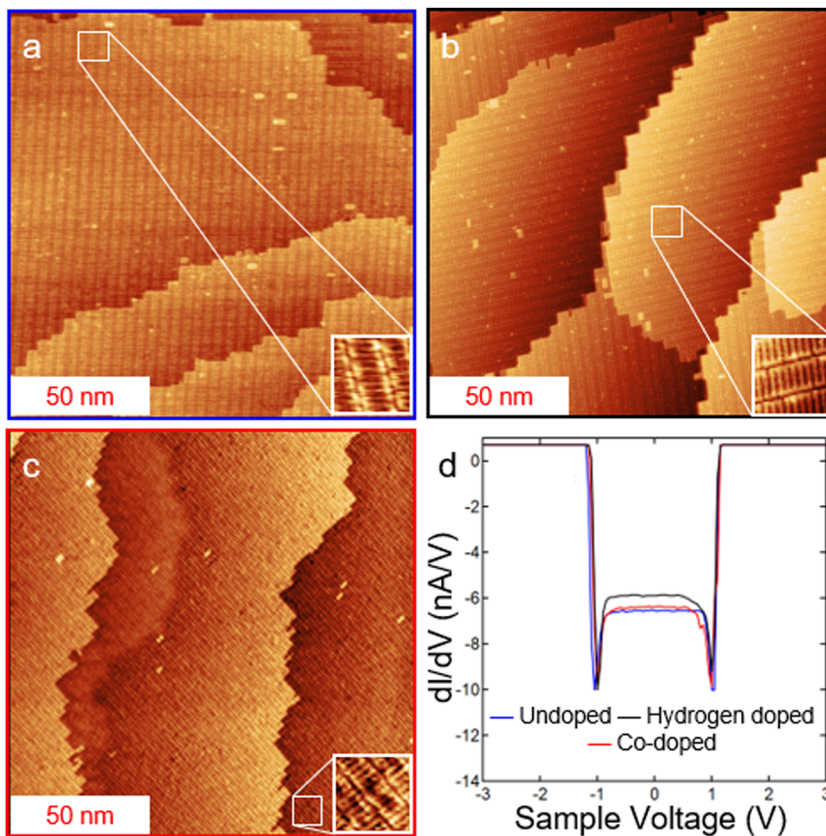


**FIG. 4.** STM images taken at  $T_{\text{STM}} = 100$  K of Nb(100)  $(3 \times 1)$ -O and corresponding STS data for (a) undoped,  $10 \times 10 \text{ nm}^2$  inset; (b) H-doped,  $10 \times 10 \text{ nm}^2$  inset; and (c) co-doped,  $10 \times 10 \text{ nm}^2$  inset. (d)  $dI/dV$  spectra for undoped (blue), H-doped (black), and co-doped (red) Nb(100) taken within hours of equilibration at  $T_{\text{STM}} = 100$  K. Imaging conditions: (a) 0.72 V, 99 pA; (b) 0.55 V, 131 pA; and (c) 14 mV, 187 pA.

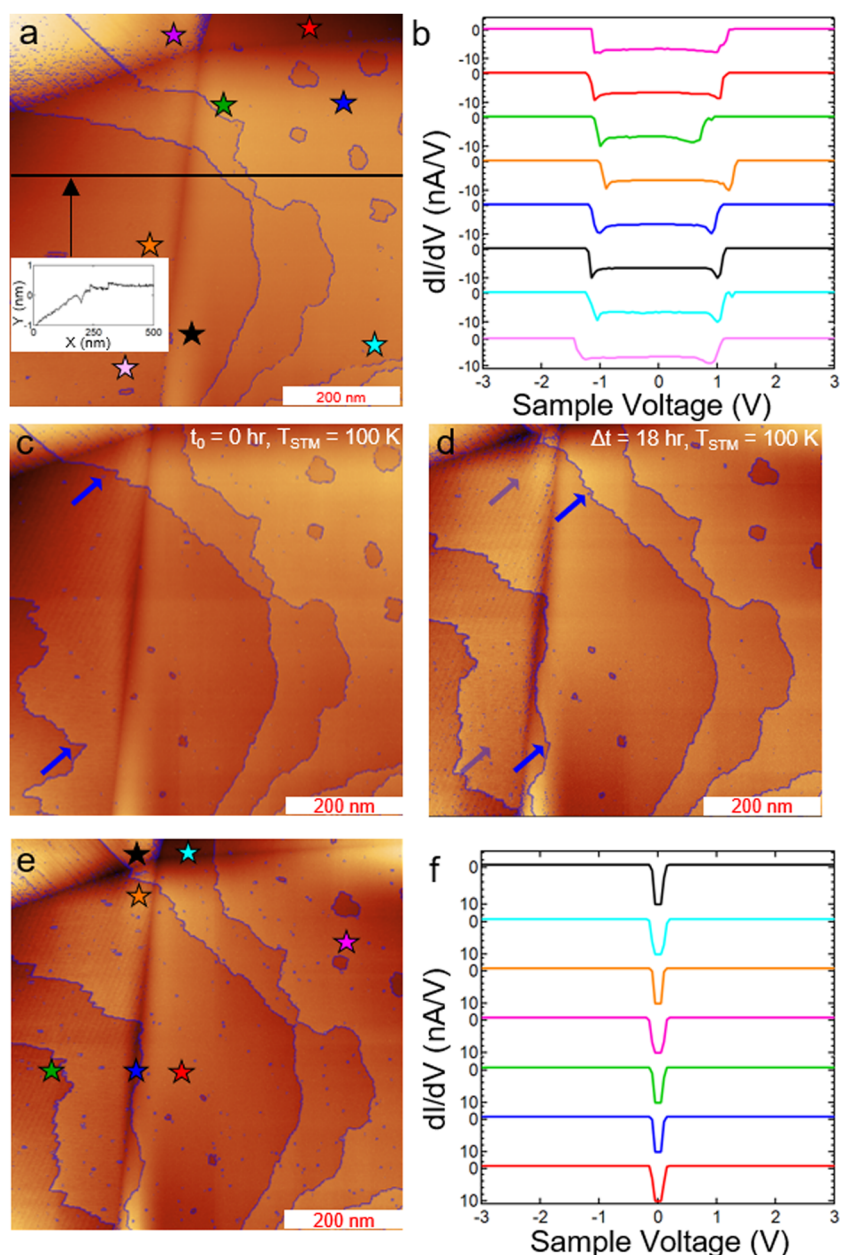


**FIG. 5.** Surface evolution of H-doped Nb(100) observed using sequential LT-STM imaging and corresponding STS measurements. (a) Faceted regions are marked with colored stars to indicate corresponding STS locations. The inset shows the facet line scan. (b) STS measurements at  $T_{\text{STM}} = 100$  K. The colored spectra correspond to the colored stars in (a). (c) Surface structure at  $t_0 = 0$ . Step edges of importance are highlighted in blue and marked with arrows. (d) Surface at  $\Delta t = 16$  h. Step migration indicated by blue arrows. (e) Surface at  $\Delta t = 16$  h with STS measurement locations marked with colored stars. (f) STS measurements corresponding to similarly colored stars in (e). Imaging conditions: (a) 0.70 V, 298 pA; (c) 101 mV, 300 pA; (d) 101 mV, 299 pA; and (e) 101 mV, 300 pA.

A region with four intersecting facets was selected for LT-STM analysis [Fig. 5(a)], with corresponding initial STS spectra [Fig. 5(b)], to thoroughly characterize the starting state of the sample. The surface DOS (SDOS) seen in Fig. 5(b), compared to the surface bandgaps in Fig. 5(d), show that no evolution has occurred following 24 h at  $T_{\text{STM}} = 100$  K. Since no evolution of the DOS has occurred, we assign  $t_0 = 0$  h in Fig. 5(c); this is useful for discussing the surface evolution as a function of time. Figure 5(c) corresponds to the surface structures present at  $t_0 = 0$  h, and step edges and etch pits of interest are masked in blue to assist the eye. Additionally,

two distinct step edges, indicated by blue arrows in Fig. 5(c), were tracked during the time-lapse STM imaging. Following  $\Delta t = 18$  h at  $T_{\text{STM}} = 100$  K, the step edges indicated with blue arrows in Fig. 5(c) have moved laterally relative to the facet, as shown in Fig. 5(e), with opaque blue arrows indicating the final position. The step edge motion relative to the facet demonstrates the positional stability of the STM measurements and confirms that the surface evolution is not an artifact of positional instability. Nb atoms do not move laterally without significant perturbation at 100 K, and the observed surface evolution is suggestive of hydride phases forming in the near

surface. It is understood that the formation of Nb hydrides imparts significant lattice strain within bulk Nb.<sup>33,38</sup> The lateral surface motion and faceting observed following H-doping and prolonged cooling at 100 K support the formation of a Nb nano-hydride species that is significantly disrupting the inherent Nb(100) lattice, resulting in the perturbation to the native Nb(100) surface reported in Figs. 5(c) and 5(d).

With the understanding that a contraction of the width of the depression in the SDOS corresponds to the presence of Nb hydrides, increase in surface resistance, and local surface heating,<sup>25</sup>  $dI/dV$  measurements were taken following the time-lapse imaging sequence at specific locations, as shown in Figs. 5(f) and 5(g). Following 72 h at  $T_{\text{STM}} = 100$  K, the SDOS was shown to significantly narrow relative to that of the native NbO across all facets within the  $500 \times 500$  nm area [Fig. 5(g)]; the contracted depression in the SDOS is  $\sim 90\%$  of that of the undoped  $(3 \times 1)$ -O surface. STS measurements employed to analyze the SDOS probes the attenuation in the surface bandgap of the  $(3 \times 1)$ -O surface oxide. The contraction of the depression in the SDOS [Fig. 5(g)] at highly faceted regions directly corresponds to the observed surface perturbation reported in Figs. 5(c) and 5(d). Due to the understanding that perturbation of Nb(100) is a result of the formation of Nb nano-hydride species imparting lattice strain, the concomitant contraction of the depression in the SDOS suggests that this is due to the formation of Nb nano-hydrides in the near-surface of the H-doped Nb(100) sample.

Once the surface evolution reported in Figs. 5(c) and 5(d) is observed, however, there is contraction of the depression in the SDOS across all areas of the surface analyzed, regardless of the surface defect density, and it is consistent across all H-doped samples analyzed. The homogeneous contraction of the depression in the SDOS could suggest the coexistence of both Nb nano-hydrides and interstitial hydrogen that are integrated into the near-surface Nb/NbO lattice. While we attribute the narrowing depression in the SDOS to the formation of Nb nano-hydrides in close enough proximity to the  $(3 \times 1)$ -O ladder surface to attenuate the NbO surface bandgap, there may also be hydrogen species that are not yet incorporated into the Nb nano-hydride participating in the evolution of the STS data.

## VII. EXPERIMENTAL AND THEORETICAL ANALYSIS OF NITROGEN DOPED Nb(100)

To determine the specific structural, chemical, and electronic effects of N-doping, the Nb(100) crystal was co-doped. Figures 6(a)–6(c) show STM images for the undoped [Fig. 6(a)], H-doped [Fig. 6(b)], and co-doped [Fig. 6(c)] samples at  $T_{\text{STM}} = 100$  K with  $(3 \times 1)$ -O ladder structures corresponding to the respective insets shown in Figs. 4(a)–4(c). Models for the surface composition of each crystal preparation were produced using DFT, as shown in Figs. 6(e) and 6(f).

In order to determine the relationship between SDOS and dopant incorporation, we report experimental and calculated STS results as  $(dI/dV)/(I/V)$ . This is to account for variation in tip-sample height differences across STS measurements and to normalize the experimental data to the calculated STS results.<sup>48</sup> Figures 6(g)–6(i) summarize both our experimental (blue lines) and

theoretical results (black, green, and, red lines) for the SDOS of undoped, H-doped, and co-doped NbO ladder surfaces. The experimental STS data show a unique electronic fingerprint for each surface structure and is supported by the calculated STS data.

The experimental STS data for all samples show a clear minimum somewhere within 0.5 eV of the Fermi level with rising DOS at higher and lower energies. This is attributable to the NbO electronic structure, which has a DOS minimum very near the Fermi level, and peaks at  $-1$  eV and  $+1.5$  eV. Because the NbO is sufficiently thin, the electronic structure of the underlying material bleeds through and perturbs the surface electronic structure slightly. Based on these perturbations, we can draw some conclusions about the chemistry of the material immediately underneath the oxide and thus better understand the chemical effect of different doping procedures.

For the experimental undoped sample SDOS, as shown in Fig. 6(g) with the blue trace, there is a broad minimum centered near or just above the Fermi level with a modest increase in SDOS at lower energies and a more significant increase in SDOS at higher energies, approaching a peak just above 1.5 eV. The H-doped sample, in contrast, has a contracted SDOS minimum at the Fermi level with a modest, roughly symmetrical increase in density of states at higher and lower energies, as shown in Fig. 6(h) by the blue trace. Finally, the co-doped preparation results in the SDOS having a minimum centered clearly below the Fermi level at approximately  $-0.5$  eV, a lower energy than either the undoped or H-doped sample, maximum centered near 1.0 eV, and another maximum centered near or below  $-1.5$  eV, as shown in Fig. 6(i) by the blue trace.

We find consistency in the observed trends between our theoretical results and the experimental signatures for all surface preparations. Our undoped SDOS calculations for the NbO surface with six (black) and nine (red) oxygen atoms per unit cell follow the observed trends of the experimental  $(dI/dV)/(I/V)$  (blue) very well near and below the Fermi level, as shown in Fig. 6(g). Small disagreement between experimental and calculated data suggests that the Nb(100)  $(3 \times 1)$ -O subsurface structure depicted in Fig. 6(d) may be more complex than currently believed; this may include either a disordered or not periodic  $(3 \times 1)$ -O cell.

Nb has a DOS minimum at around 1 eV and a maximum just below the Fermi level. In contrast, the  $\beta$  hydride phase, which has been previously observed following Nb nano-hydride formation,<sup>12,17</sup> has a DOS minimum just below the Fermi level and a generally flat DOS profile. The small but noticeable negative shift in the minimum of the  $dI/dV/(I/V)$  scan in the H-doped sample [Fig. 6(h)] and the non-observation of large DOS variations are therefore tentatively consistent with the replacement of sub-surface Nb with sub-surface NbH. The full slab calculation for the ladder structure SDOS with subsurface  $\beta$  hydride, shown in Fig. 6(e), shows the anticipated effect with a lower energy minimum and a flatter overall profile. Differences between experimental and theoretical data may be due to the positioning of individual hydrogen interstitials as it is unlikely that we reproduced the complex hydride structure to that level of precision.

The DOS of NbN rises monotonically with the energy in the range  $-1.5$  eV to  $+1.5$  eV. The N-doped sample, however, has a very prominent DOS peak at  $-1.5$  eV [Fig. 6(i)]. Therefore, the data are not consistent with the replacement of sub-surface Nb with



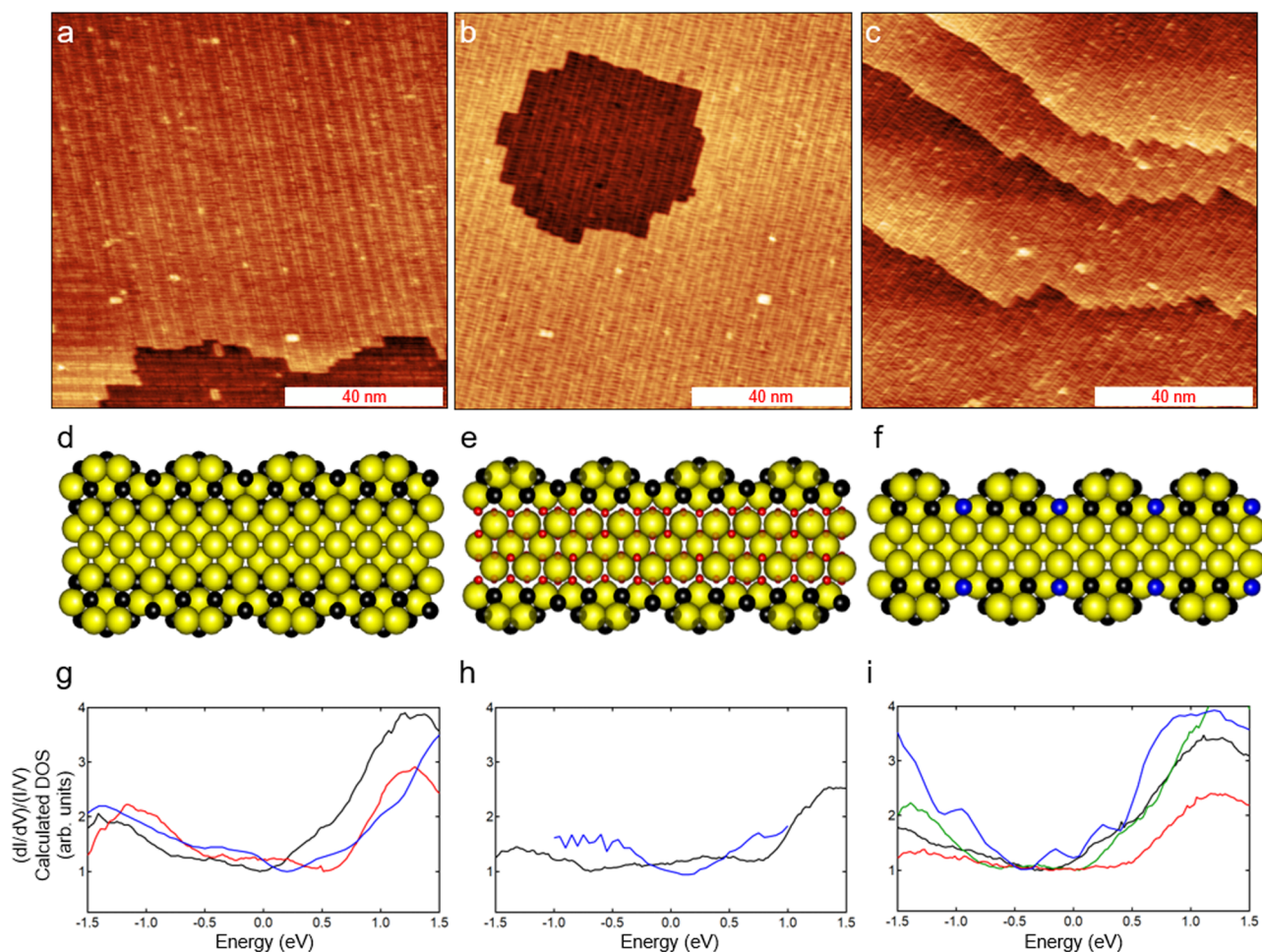


**FIG. 6.** STM and STS analysis of Nb nano-hydride growth and suppression. Images taken after  $\sim 72$  h at  $T_{\text{STM}} = 100$  K: (a) undoped Nb(100) ( $3 \times 1$ )-O, (b) H-doped Nb(100), and (c) co-doped Nb(100). (d) 3-layer oxide model for undoped Nb(100) ( $3 \times 1$ )-O. (e) Model for the H-doped surface. Nb atoms are slightly transparent to clarify positions of H atoms (red) in the  $\beta$  hydride phase. (f) Model for the N-doped surface; nitrogen atoms (blue) as substitutional defects. (g) Experimental (blue) and calculated surface density of states for the undoped Nb(100) sample for six oxygen atoms per unit cell (black) and nine oxygen atoms per unit cell (red). (h) Experimental (blue) and calculated surface density of states for H-doped Nb(100) showing a  $\beta$  hydride phase. (i) Experimental (blue) and calculated surface density of states for co-doped Nb(100) with nitrogen substitutional defects (green), nitrogen interstitials (black), and an ordered nitride phase (red). Imaging conditions: (a) 0.72 V, 99 pA; (b) 101 mV, 300 pA; and (c)  $-0.83$  V, 89 pA.

sub-surface NbN, and our slab calculation bears this out. We then suspect some more subtle changes involving incorporation of nitrogen into the ladder structure oxide; such calculations give a SDOS in significantly better agreement with the experiment than the sub-surface NbN model. In particular, our calculated SDOS for the oxide surface with a nitrogen substitutional defect, shown in Fig. 6(f), shows nice agreement with the experimentally observed trends in STS measurements on the co-doped sample, shown in Fig. 6(i). This result aligns with our intuition for the kinetics of nitrogen diffusion into the NbO ( $3 \times 1$ )-O ladder structure surface as this site represents the most straightforward pathway through the oxide. Interestingly, calculations involving higher concentrations of nitrogen, such as an additional nitrogen interstitial (black) or an ordered nitride phase

(red), show worse agreement with the experimental data. This suggests that the preparation method results in nitrogen diffusion into the bulk of the material as opposed to a higher concentration of nitrogen in the near surface. Therefore, we conclude that interstitial nitrogen, rather than an ordered nitride phase, plays an important role in preventing hydride phases from forming at the surface. This supports previous first principles calculations suggest that the presence of interstitial nitrogen increases the diffusion barrier for hydrogen and the formation energy for niobium hydrides. The hypothesis that interstitial nitrogen inhibits hydrogen diffusion also aligns with our observation that a higher pressure is necessary for H-doping following N-doping in order to reach the same H-doping level.<sup>49</sup>

## VIII. CONCLUSION

One of the main limiting factors in reaching the theoretical performance limits of Nb based SRF cavities is due to the “Q disease” at high fields due to the presence of Nb hydrides. N-doping is known to suppress Nb hydride growth, resulting in consistently higher  $Q$  and decreased  $R_s$ . Despite these advances in cavity fabrication, further understanding of the growth and suppression mechanisms of Nb hydrides due to nitrogen doping is needed. In this work, combined experimental and theoretical results provide the first *in situ* temporally and spatially resolved structural and electronic analysis of Nb(100) as a function of Nb nano-hydride growth and suppression due to N-doping. Using sequential LT-STM imaging, we have observed growth of Nb nano-hydrides in real-time with nanoscale spatial resolution. The electronic structure, and corresponding near-surface phase, of undoped, H-doped, and co-doped Nb(100) was identified via DFT calculations and supported with spatially resolved STS measurements of the Nb(100) surface.

STS and DFT data of H-doped Nb(100) show a distinct change in electronic characteristics corresponding to a narrowing of the depression in the SDOS due to the formation of a distinct near-surface Nb nano-hydride phase. In stark contrast, the co-doped Nb(100) does not exhibit a narrowing in the depression in the SDOS. Rather, the depression widens relative to that of the undoped samples following  $\sim 72$  h at  $T_{STM} = 100$  K. This suggests that a unique nitrogen induced phase is present upon co-doping that beneficially affects the surface properties of Nb via the suppression of Nb hydrides on the nanoscale and continuing thereafter. Calculated SDOS for each sample preparation are consistent with the experimentally obtained STS data, supporting the spatially resolved experimental electronic characterization.

The observed structural and electronic evolution of undoped, H-doped, and N-doped Nb(100) provides significant insight into the mechanistic effects of N doping and related Nb hydride suppression in real-time with nanoscale spatial resolution. These results broaden our understanding of Nb hydride growth and suppression as a result of N-doping and provide needed guidance to further optimize Nb doping, information essential to realizing further advances in superconducting material performance for SRF-based accelerators and related free electron light sources.

## AUTHORS' CONTRIBUTION

R.D.V. and R.G.F. contributed equally to this work and are co-first authors of this paper.

## ACKNOWLEDGMENTS

This work was supported by the U.S. National Science Foundation under Award No. PHY-1549132, and the Center for Bright Beams. R.D.V. thanks the Fermi National Accelerator Laboratory and The University of Chicago for partial fellowship support during this work. R.G.F. thanks The University of Chicago for partial support via the Kadanoff-Rice Fellowship during this work.

This work was dedicated to all current and former women in the Sibener Group. The scientific creativity and accomplishments of

these women, including 21 graduate students, 5 postdoctoral scholars, 13 undergraduate students, and 4 high school students, have directly contributed to our broader understanding of interfacial phenomena in both the Sibener group at The University of Chicago and the scientific community at large.

## DATA AVAILABILITY

The data that support the findings of this study are available within the article.

## REFERENCES

- <sup>1</sup>H. Padamsee, *RF Superconductivity: Science, Technology, and Applications* (Wiley VCH, Weinheim, 2009).
- <sup>2</sup>H. Padamsee, *Supercond. Sci. Technol.* **14**, R28 (2001).
- <sup>3</sup>C. Antoine, *Materials and Surface Aspects in the Development of SRF Niobium Cavities*, EuCARD Editorial Series on Accelerator Science (EuCARD Publication, 2012).
- <sup>4</sup>D. K. Finnemore, T. F. Stromberg, and C. A. Swenson, *Phys. Rev.* **149**, 231 (1966).
- <sup>5</sup>A. Daccà, G. Gemme, L. Mattera, and R. Parodi, *Appl. Surf. Sci.* **126**, 219 (1998).
- <sup>6</sup>H. H. Farrell and M. Strongin, *Surf. Sci.* **38**, 18 (1973).
- <sup>7</sup>H. H. Farrell, H. S. Isaacs, and M. Strongin, *Surf. Sci.* **38**, 31 (1973).
- <sup>8</sup>A. Grassellino, A. Romanenko, D. Sergatskov, O. Melnychuk, Y. Trenikhina, A. Crawford, A. Rowe, M. Wong, T. Khabiboulline, and F. Barkov, *Supercond. Sci. Technol.* **26**, 102001 (2013).
- <sup>9</sup>A. Romanenko, A. Grassellino, F. Barkov, and J. P. Ozelis, *Phys. Rev. Spec. Top. - Accel. Beams* **16**, 012001 (2013).
- <sup>10</sup>Y. Trenikhina, A. Grassellino, O. Melnychuk, and A. Romanenko, in *Proceedings of SRF2015* (JACoW, Geneva, Switzerland, 2015), p. 223.
- <sup>11</sup>P. Dhakal, G. Ciovati, P. Kneisel, and G. R. Myneni, *IEEE Trans. Appl. Supercond.* **25**, 1 (2015).
- <sup>12</sup>Y. Trenikhina, A. Romanenko, J. Kwon, J.-M. Zuo, and J. F. Zasadzinski, *J. Appl. Phys.* **117**, 154507 (2015).
- <sup>13</sup>N. R. Groll, G. Ciovati, A. Grassellino, A. Romanenko, J. F. Zasadzinski, and T. Proslir, [arXiv:1805.06359](https://arxiv.org/abs/1805.06359) [cond-mat. sup-con.] (2018).
- <sup>14</sup>F. Barkov, A. Romanenko, Y. Trenikhina, and A. Grassellino, *J. Appl. Phys.* **114**, 164904 (2013).
- <sup>15</sup>A. Romanenko, F. Barkov, L. D. Cooley, and A. Grassellino, *Supercond. Sci. Technol.* **26**, 035003 (2013).
- <sup>16</sup>F. Barkov, A. Romanenko, and A. Grassellino, *Phys. Rev. Spec. Top. - Accel. Beams* **15**, 122001 (2012).
- <sup>17</sup>R. Tao, A. Romanenko, L. D. Cooley, and R. F. Klie, *J. Appl. Phys.* **114**, 044306 (2013).
- <sup>18</sup>C. Z. Antoine and S. Berry, *AIP Conf. Proc.* **671**, 176 (2003).
- <sup>19</sup>J. Knobloch, *AIP Conf. Proc.* **671**, 133 (2003).
- <sup>20</sup>B. Bonin and R. W. Roth, in *Proceedings of the 5th Workshop on RF Superconductivity* (JACoW, Geneva, Switzerland, 1991), p. 210.
- <sup>21</sup>C. Z. Antoine, B. Aune, B. Bonin, J. Cavedon, M. Juillard, A. Godin, C. Henriot, P. Leconte, H. Safa, A. Veyssiere, A. Chevarier, and B. Roux, in *Proceedings of the 5th Workshop on RF Superconductivity* (JACoW, Geneva, Switzerland, 1991), p. 616.
- <sup>22</sup>E. Fromm and H. Jehn, *Metall. Mater. Trans. B* **3**, 1685 (1972).
- <sup>23</sup>S. Giordano, H. Hahn, H. J. Halama, C. Varmazis, and L. Rinderer, *J. Appl. Phys.* **44**, 4185 (1973).
- <sup>24</sup>D. Gonnella, J. Kaufman, and M. Liepe, *J. Appl. Phys.* **119**, 073904 (2016).
- <sup>25</sup>M. Martinello, A. Grassellino, M. Checchin, A. Romanenko, O. Melnychuk, D. A. Sergatskov, S. Posen, and J. F. Zasadzinski, *Appl. Phys. Lett.* **109**, 062601 (2016).
- <sup>26</sup>R. Musenich, P. Fabbriatore, G. Gemme, R. Parodi, M. Viviani, B. Zhang, V. Buscaglia, and C. Bottino, *J. Alloys Compd.* **209**, 319 (1994).

- <sup>27</sup>G. Pfeiffer and H. Wipf, *J. Phys. F: Met. Phys.* **6**, 167 (1976).
- <sup>28</sup>A. I. Shirley, C. K. Hall, and N. J. Prince, *Acta Metall.* **31**, 985 (1983).
- <sup>29</sup>P. Garg, S. Balachandran, I. Adlakha, P. J. Lee, T. R. Bieler, and K. N. Solanki, *Supercond. Sci. Technol.* **31**, 115007 (2018).
- <sup>30</sup>D. A. Gonnella, "The fundamental science of nitrogen-doping of niobium superconducting cavities," Ph.D. thesis, Cornell University, 2016.
- <sup>31</sup>A. Grassellino, A. Romanenko, S. Posen, Y. Trenikhina, O. Melnychuk, D. A. Sergatskov, and M. Merio, in *Proceedings of SRF2015* (JACoW, Geneva, Switzerland, 2015), p. 48.
- <sup>32</sup>A. Grassellino, A. Romanenko, Y. Trenikhina, M. Checchin, M. Martinello, O. S. Melnychuk, S. Chandrasekaran, D. A. Sergatskov, S. Posen, A. C. Crawford, S. Aderhold, and D. Bice, *Supercond. Sci. Technol.* **30**, 094004 (2017).
- <sup>33</sup>D. C. Ford, L. D. Cooley, and D. N. Seidman, *Supercond. Sci. Technol.* **26**, 105003 (2013).
- <sup>34</sup>S. Posen and M. Liepe, *Phys. Rev. Spec. Top. - Accel. Beams* **17**, 112001 (2014).
- <sup>35</sup>J. T. Maniscalco, D. Gonnella, and M. Liepe, *J. Appl. Phys.* **121**, 043910 (2017).
- <sup>36</sup>C. Benvenuti, S. Calatroni, I. E. Campisi, P. Darriulat, M. A. Peck, R. Russo, and A.-M. Valente, *Physica C* **316**, 153 (1999).
- <sup>37</sup>J. Halbritter, *Z. Phys.* **238**, 466 (1970).
- <sup>38</sup>D. C. Ford, L. D. Cooley, and D. N. Seidman, *Supercond. Sci. Technol.* **26**, 095002 (2013).
- <sup>39</sup>D. C. Ford, P. Zapol, and L. D. Cooley, *J. Phys. Chem. C* **119**, 14728 (2015).
- <sup>40</sup>Z. C. Szkopiak and L. W. Derry, *J. Nucl. Mater.* **13**, 130 (1964).
- <sup>41</sup>Z. C. Szkopiak and A. P. Miodownik, *J. Nucl. Mater.* **17**, 20 (1965).
- <sup>42</sup>D. Gonnella, R. Eichhorn, F. Furuta, M. Ge, D. Hall, V. Ho, G. Hoffstaetter, M. Liepe, T. O'Connell, S. Posen, P. Quigley, J. Sears, V. Veshcherevich, A. Grassellino, A. Romanenko, and D. A. Sergatskov, *J. Appl. Phys.* **117**, 023908 (2015).
- <sup>43</sup>A. Romanenko, A. Grassellino, O. Melnychuk, and D. A. Sergatskov, *J. Appl. Phys.* **115**, 184903 (2014).
- <sup>44</sup>R. D. Veit, N. A. Kautz, R. G. Farber, and S. J. Sibener, *Surf. Sci.* **688**, 63 (2019).
- <sup>45</sup>Y. Li, B. An, S. Fukuyama, K. Yokogawa, and M. Yoshimura, *Mater. Charact.* **48**, 163 (2002).
- <sup>46</sup>B. An, S. Fukuyama, K. Yokogawa, and M. Yoshimura, *Phys. Rev. B* **68**, 115423 (2003).
- <sup>47</sup>R. Sundararaman, K. Letchworth-Weaver, K. A. Schwarz, D. Gunceler, Y. Ozhabes, and T. A. Arias, *SoftwareX* **6**, 278 (2017).
- <sup>48</sup>P. Mårtensson and R. M. Feenstra, *Phys. Rev. B* **39**, 7744 (1989).
- <sup>49</sup>N. Marzari and D. Vanderbilt, *Phys. Rev. B* **56**, 12847 (1997).
- <sup>50</sup>V. B. Braginsky, V. P. Mitrofanov, V. I. Panov, and J. H. Hetherington, *Acoust. Soc. Am. J.* **81**, 1652 (1987).
- <sup>51</sup>J. P. Perdew, K. Burke, and M. Ernzerhof, *Phys. Rev. Lett.* **77**, 3865 (1996).
- <sup>52</sup>K. F. Garrity, J. W. Bennett, K. M. Rabe, and D. Vanderbilt, *Comput. Mater. Sci.* **81**, 446 (2014).
- <sup>53</sup>N. Marzari, D. Vanderbilt, A. De Vita, and M. C. Payne, *Phys. Rev. Lett.* **82**, 3296 (1999).
- <sup>54</sup>H. Oechsner, J. Giber, H. J. Füsler, and A. Darlinski, *Thin Solid Films* **124**, 199 (1985).
- <sup>55</sup>I. Arfaoui, J. Cousty, and C. Guillot, *Surf. Sci.* **557**, 119 (2004).
- <sup>56</sup>L. H. Rovner, A. Drowart, F. Degreve, and J. Drowart, Air Force Materials Laboratory Technical Report No. AFML-TR-68-200, 1968.
- <sup>57</sup>Y. Uehara, T. Fujita, M. Iwami, and S. Ushioda, *Surf. Sci.* **472**, 59 (2001).
- <sup>58</sup>S. Usami, N. Tominaga, and T. Nakajima, *Vacuum* **27**, 11 (1977).
- <sup>59</sup>N. Greenwood and A. Earnshaw, *Chemistry of the Elements*, 2nd ed. (Butterworth-Heinemann, Oxford, 1997).
- <sup>60</sup>P. H. Dawson and W.-C. Tam, *Surf. Sci.* **81**, 464 (1979).
- <sup>61</sup>K. H. Rieder, *Appl. Surf. Sci.* **4**, 183 (1980).
- <sup>62</sup>Z. Q. Yang, L. Lin, X. Y. Lu, W. W. Tan, D. Y. Yang, and J. Zhao, in *Proceedings of SRF2015* (JACoW, Geneva, Switzerland, 2015), p. 169.
- <sup>63</sup>A. Romanenko and H. Padamsee, *Supercond. Sci. Technol.* **23**, 045008 (2010).
- <sup>64</sup>Z.-H. Sung, M. Wang, A. A. Polyanskii, C. Santosh, S. Balachandran, C. Compton, D. C. Larbalestier, T. R. Bieler, and P. J. Lee, *J. Appl. Phys.* **121**, 193903 (2017).